

# Variable Absorption Line in XTE J1810–197

Eda Vurgun<sup>1\*</sup>, Manoneeta Chakraborty<sup>2,3</sup>, Tolga Güver<sup>4,5</sup> and  
Ersin Göğüş<sup>2</sup>

<sup>1</sup>*Istanbul University, Graduate School of Science and Engineering, Department of Astronomy and Space Sciences, 34116, Beyazıt, İstanbul, Turkey*

<sup>2</sup>*Sabancı University, Faculty of Engineering and Natural Sciences, Tuzla, 34956, İstanbul, Turkey*

<sup>3</sup>*Center of Astronomy, Indian Institute of Technology Indore, Khandwa Road, Simrol Indore 453552, India*

<sup>4</sup>*Istanbul University, Science Faculty, Department of Astronomy and Space Sciences, 34119, Beyazıt, İstanbul, Turkey*

<sup>5</sup>*Istanbul University, Observatory Research and Application Center, Istanbul University, 34119, İstanbul, Turkey*

★E – mail : [eda.vurgun@ogr.iu.edu.tr](mailto:eda.vurgun@ogr.iu.edu.tr)

---

## Abstract

We report the results of a long-term spectral and timing study of the first transient magnetar, XTE J1810–197 which was discovered in 2003, when its X-ray luminosity increased  $\approx 100$  fold. We fit X-ray spectra of all archival X-ray observations using a two-component blackbody model, where the cool component is most likely originating from the whole surface of the neutron star and the hot component is from a much smaller hot spot. We investigate the long-term evolution of the surface emission characteristics via tracing its surface temperature, apparent emitting area and pulsed fraction. We evaluate the pulsed fraction in two energy intervals ( $< 1.5$  keV and  $> 1.5$  keV) and show that the XTE J1810–197 exhibits slightly higher pulsed emission at energies above 1.5 keV. We explore the characteristics of an absorption line detected around 1.1 keV. We find that the absorption feature is highly variable and its profile is asymmetric. To accurately represent this feature, we introduced an asymmetric Gaussian profile, and quantified the level of asymmetry of the absorption feature.

*Keywords:* stars: neutron, magnetar, absorption line, XTE J1810–197

---

## 1. Introduction

Anomalous X-ray Pulsars (AXPs) and Soft-Gamma Repeaters (SGRs) are a group of neutron stars, which differ from others because of their numerous observational properties. These objects have relatively long spin periods ( $> 2$  s) and high inferred period derivatives ( $10^{-13} - 10^{-11}$  s/s) leading to dipole magnetic fields at the surface, of the order of  $10^{14-15}$  G. These temporal properties, along with the observed energetic short X-ray bursts and giant flares from these objects led to the suggestion that AXPs and SGRs are magnetars (Duncan, 1992, 1996); objects whose persistent X-ray luminosity arises from the decay of a superstrong magnetic field.

Although the first discovered AXPs and SGRs were persistent and relatively bright X-ray sources, today the McGill Online Magnetar Catalog<sup>1</sup> (Olausen, 2014) consists of nine transient objects out of 23 confirmed AXPs and SGRs. All known magnetars exhibit a wide range of temporal variations, such as bursts, glitches, and outbursts. Transient Anomalous X-ray Pulsars (TAXPs) display distinct bursts and/or outbursts, which are characterized by an abrupt increase in X-ray flux, followed by a long-term flux decay (Kaspi, 2007).

XTE J1810–197 is the prototypical TAXP, which was first discovered in 2003 by Ibrahim (2004), when its X-ray luminosity increased suddenly by  $\approx 100$  times compared to its quiescent state (Halpern, 2005). Since its discovery, the X-ray flux of the source declined exponentially and it is now thought to be in a quiescent phase (Gotthelf, 2007). XTE J1810–197 has a spin period of 5.54 s period and a large period derivative  $10^{-11}$  s/s (Ibrahim, 2004). These timing properties imply a surface dipole magnetic field strength of  $2 - 3 \times 10^{14}$  G, which is independently confirmed

---

<sup>1</sup><http://www.physics.mcgill.ca/pulsar/magnetar/main.html>

by Güver (2007) using an X-ray spectral model that take into account the radiative processes taking place in the atmosphere of a magnetar and its magnetosphere. Güver (2007) also found that the X-ray spectra of the source obtained with XMM-Newton until 2006 could be well modeled with the cooling of a roughly constant area hot spot.

Thanks to extensive observing campaigns performed with Chandra X-ray Observatory and XMM-Newton the spectral and timing evolution of XTE J1810–197 has been followed in a unique and detailed way (Alford, 2016; Pintore, 2016). Alford (2016) modeled the X-ray spectra with two or three blackbody components, where the coldest component is held fixed throughout all the observations. They found that the hot spot remains on the surface with a 0.3 keV temperature, and hence the pulsations. Similar to Bernardini (2009), Alford (2016) report the presence of a spectral feature at 1.2 keV at all epochs, which if assumed to be a proton cyclotron line indicates a magnetic field strength of approximately  $2 \times 10^{14}$  G, in agreement with earlier conclusions. Pintore (2016) investigated the evolution of the pulsar spin period and found evidence for two distinct regimes. During the decay from the outburst  $\dot{v}$  was found to be highly variable; only about 3000 days after its outburst onset it was possible to phase connect. They also report a possible anti-glitch at around MJD 55400. In another recent study on XTE J1810–197, Camilo (2016) reported timing and polarimetric observations of the source using the Green Bank, Nançay and Parkes radio telescopes. Radio pulsation was detected during the observations performed between 2006–2008, which coincide with the times of the frequency change reported by Pintore (2016). In this time interval, unlike ordinary radio pulsars the pulsation had a large day-to-day fluctuation, which resulted in a steep radio spectrum, rather than a flat-spectrum. Camilo (2016) also reported that XTE J1810–197 has not been detected in the radio band since 2008.

In this paper we report on the spectral and timing evolution of the XTE J1810–197 spanning more than 12 years. Our systematic investigation focuses on modeling its spectral continuum with two blackbody functions, and a better understanding of the spectral feature at 1.2 keV with an asymmetric Gaussian function. We describe the observations of XTE J1810–197 used in our analysis in §2. In §3 and §4 we present the details of our temporal and spectral analysis. In §5, we present the results of absorption line structure. In §6, we discuss the implications of our results.

## 2. Observations and Data Analysis

We employed 34 archival observations of XTE J1810–197 collected with Chandra X-ray Observatory and XMM-Newton. Table 1 lists the log of these observations. We present the details of our data reduction methodology for each instrument separately.

### 2.1. Chandra X-ray Observatory

There are a total of 14 Chandra observations performed between 2006 and 2015. Out of these, 12 were performed with the Advanced CCD Imaging Spectrometer (ACIS) and 2 of them were performed using the High Resolution Camera (HRC). Since the HRC does not provide fine spectral resolution, we employed only the Chandra observations performed with ACIS. We used CIAO and CALDB version 4.5, 4.5.5.1 for the calibration of the data. For the last two observations (15870 and 15871), we used CIAO and CALDB version 4.6, 4.6.3. We extracted each spectrum using the *specextract* tool following the standard Chandra data analysis threads with a 6 arcsec extraction radius for source and 7 arcsec for background regions. Response and ancillary response files were generated using the *mkacisrmf* and *mkarf* tools, respectively. We grouped the resulting spectra so that each spectral channel contains a minimum of 50 counts. Often the time resolution provided by the Chandra data was  $\sim 0.4$  s, which usually correspond to 1/8 sub-array mode of ACIS.

### 2.2. XMM-Newton

We inspected all 22 X-ray datasets obtained with the EPIC-pn detector between 2003 and 2014. We did not employ one exposure (ID : 0552800301) because of its high solar particle background. We performed the calibration of the data using the Science Analysis Software (SAS) version 12.0.1. The calibrated and cleaned event files were created using the *epproc* task. We used the *rmfgen* and *arfgen* tools within SAS to generate the response files. All X-ray spectra were grouped to have at least 50 counts in each spectral energy bin and not to oversample the instrumental energy resolution by more than a factor of three, using the *specgroup* tool. The time resolution offered by EPIC-pn data is 48 ms and 73 ms for the large window and full frame sub-modes, respectively.

Table 1: Log of archival X-ray observations.

#	Observatory	Observation ID	Start Time MJD	Date UT	Exp. Time ks	Data Mode
1	XMM-Newton	0161360301	52890.55714	2003 Sep 8	6.1	Small Window
2	XMM-Newton	0161360401	52890.70589	2003 Sep 8	0.3	Small Window
3	XMM-Newton	0161360501	53075.49562	2004 Mar 11	8.9	Large Window
4	XMM-Newton	0164560601	53266.49812	2004 Sep 18	20.9	Full Window
5	XMM-Newton	0301270501	53447.99696	2005 Mar 18	30.5	Large Window
6	XMM-Newton	0301270401	53633.44414	2005 Sep 20	26.5	Large Window
7	XMM-Newton	0301270301	53806.79024	2006 Mar 12	19.2	Large Window
8	Chandra	6660	53988.80975	2006 Sep 10	27.4	VFAINT
9	XMM-Newton	0406800601	54002.06184	2006 Sep 24	37.9	Large Window
10	XMM-Newton	0406800701	54165.77228	2007 Mar 6	32.9	Large Window
11	XMM-Newton	0504650201	54359.06106	2007 Sep 16	67.0	Large Window
12	Chandra	7594	54543.00393	2008 Mar 18	26.9	VFAINT
13	XMM-Newton	0552800201	54895.65530	2009 Mar 5	39.8	Large Window
14	XMM-Newton	0605990201	55079.62303	2009 Sep 5	17.9	Large Window
15	XMM-Newton	0605990301	55081.55238	2009 Sep 7	16.3	Large Window
16	XMM-Newton	0605990401	55097.70535	2009 Sep 23	11.0	Large Window
17	Chandra	11102	55136.66053	2009 Nov 1	22.8	VFAINT
18	Chandra	12105	55242.69038	2010 Feb 15	11.4	VFAINT
19	Chandra	11103	55244.74581	2010 Feb 17	11.5	VFAINT
20	XMM-Newton	0605990501	55295.18394	2010 Apr 9	7.1	Large Window
21	Chandra	12221	55354.13126	2010 Jun 7	9.5	FAINT
22	XMM-Newton	0605990601	55444.67699	2010 Sep 5	8.4	Large Window
23	Chandra	13149	55494.16719	2010 Oct 25	14.6	FAINT
24	Chandra	13217	55600.99240	2011 Feb 8	13.6	FAINT
25	XMM-Newton	0671060101	55654.08608	2011 Apr 3	14.3	Large Window
26	XMM-Newton	0671060201	55813.38491	2011 Sep 9	11.8	Large Window
27	Chandra	13746	55976.37662	2012 Feb 19	18.2	VFAINT
28	Chandra	13747	56071.35995	2012 May 24	18.2	VFAINT
29	XMM-Newton	0691070301	56176.98015	2012 Sep 6	14.6	Large Window
30	XMM-Newton	0691070401	56354.19799	2013 Mar 3	7.4	Large Window
31	XMM-Newton	0720780201	56540.85575	2013 Sep 5	18.8	Large Window
32	Chandra	15870	56717.31190	2014 Mar 1	18.2	VFAINT
33	XMM-Newton	0720780301	56720.97152	2014 Mar 4	19.6	Large Window
34	Chandra	15871	56907.94909	2014 Sep 7	18.2	VFAINT

### 3. Temporal Analysis

For the timing analysis, we investigated the timing features like pulsed fraction for the observations listed in Table 2. We extracted the photon arrival times for the XMM-Newton and Chandra data and performed barycentric corrections on them using the position coordinates from VLBA observations (Helfand, 2007). A long term phase connected timing solution could not be obtained for this source due to data constraints (Pintore, 2016; Camilo, 2016). Therefore, for each observation, we calculated the local spin frequency of pulsar using the  $Z_n^2$  statistic (Buccheri, 1983). This statistic is defined as

$$Z_n^2 = (2/N)\Sigma_k^n ((\Sigma_j^N \cos k\phi_j)^2 + (\Sigma_j^N \sin k\phi_j)^2) \quad (1)$$

where  $\phi$  is the phase array,  $N$  is the number of trial phase bins and  $n$  is the number of harmonics. We created a  $Z_n^2$  power distribution for a number of trial frequencies ranging from 1.0/5.55 to 1.0/5.53 Hz with frequency steps of  $10^{-7}$  Hz and taking the value of  $n$  to be 2. The phases were calculated by multiplying the barycenter corrected times by each trial frequency, which were used to compute the  $Z_n^2$  value for each frequency. We identified the frequency corresponding to the peak of the  $Z_n^2$  power distribution as the local spin frequency corresponding to that particular observation. The obtained frequencies match closely with that reported in the literature (Camilo, 2016). Using this estimated frequency for each observation, we folded the data at this frequency and obtained the pulse profiles. In order to examine the temporal evolution with energy, the profiles were obtained in two energy ranges 0.5-1.5 and 1.5-10.0 keV (as chosen based on the BB components from the spectral analysis). From the profiles in the two energy ranges, we subtracted the background contribution and calculated the pulse fraction. We defined the pulsed fraction as

$$PF = ((1/N) * (\Sigma_i^N (R_i - R_{avg})^2 - \Delta R_i^2))^{1/2} / R_{avg} \quad (2)$$

where  $R_i$  is the count rate in  $i^{\text{th}}$  phase bin in the pulse profile,  $\Delta R_i$  is the corresponding error,  $R_{\text{avg}}$  is the average count rate in the pulse profile and  $N$  is the number of phase bins. Following the above procedure, we obtained the time evolution of the rms pulsed fraction in two energy ranges using both *XMM-Newton* and *Chandra* data which is shown in the last panel of [Figure 1](#) and [Table 2](#).

Table 2: Pulsed fractions of XTE J1810–197 in two energy bands

#	Pulsed Fraction (0.5–1.5 keV)	Pulsed Fraction (1.5–10.0 keV)
1	$0.319 \pm 0.007$	$0.408 \pm 0.005$
2	$0.349 \pm 0.018$	$0.537 \pm 0.015$
3	$0.239 \pm 0.008$	$0.329 \pm 0.006$
4	$0.228 \pm 0.006$	$0.342 \pm 0.005$
5	$0.199 \pm 0.006$	$0.298 \pm 0.006$
6	$0.149 \pm 0.009$	$0.222 \pm 0.011$
7	$0.154 \pm 0.012$	$0.235 \pm 0.018$
8	$0.127 \pm 0.016$	$0.257 \pm 0.025$
9	$0.157 \pm 0.009$	$0.276 \pm 0.016$
10	$0.123 \pm 0.011$	$0.255 \pm 0.028$
11	$0.157 \pm 0.007$	$0.251 \pm 0.013$
12	$0.173 \pm 0.027$	$0.328 \pm 0.047$
13	$0.151 \pm 0.009$	$0.272 \pm 0.022$
14	$0.157 \pm 0.015$	$0.322 \pm 0.034$
15	$0.147 \pm 0.015$	$0.261 \pm 0.038$
16	$0.161 \pm 0.020$	$0.332 \pm 0.048$
17	$0.183 \pm 0.019$	$0.300 \pm 0.037$
18	$0.122 \pm 0.037$	$0.282 \pm 0.057$
19	$0.132 \pm 0.038$	$0.292 \pm 0.056$
20	$0.137 \pm 0.028$	$0.202 \pm 0.095$
21	$0.144 \pm 0.039$	$0.217 \pm 0.075$
22	$0.153 \pm 0.023$	$0.300 \pm 0.054$
23	$0.152 \pm 0.028$	$0.302 \pm 0.046$
24	$0.195 \pm 0.027$	$0.328 \pm 0.049$
25	$0.184 \pm 0.016$	$0.303 \pm 0.039$
26	$0.177 \pm 0.018$	$0.416 \pm 0.049$
27	$0.149 \pm 0.025$	$0.326 \pm 0.039$
28	$0.179 \pm 0.024$	$0.310 \pm 0.039$
29	$0.153 \pm 0.016$	$0.336 \pm 0.036$
30	$0.145 \pm 0.026$	$0.378 \pm 0.054$
31	$0.129 \pm 0.014$	$0.349 \pm 0.032$
32	$0.225 \pm 0.024$	$0.366 \pm 0.041$
33	$0.167 \pm 0.013$	$0.319 \pm 0.029$
34	$0.174 \pm 0.027$	$0.328 \pm 0.047$

#### 4. Spectral Analysis

We performed spectral analysis in the 0.5–10.0 keV energy range using Xspec 12.8.2q and 12.10.0c ([Arnaud, 1996](#)). X-ray spectra of XTE J1810–197 have generally been interpreted with multiple blackbody functions. [Alford \(2016\)](#) employed three blackbody functions for those observations performed during the first 2.5 years after the outburst and used two blackbodies for the rest. We tested the statistical necessity of adding a third blackbody to the data via Monte Carlo simulations and applying F-test. In particular, we generated 1000 simulated spectra using two blackbody functions as the seed model, and fit them with three blackbody functions, as well as two blackbody functions. We find that the change in  $\chi^2$  of the three blackbodies were not significant. Thus, we conclude that the addition of the third blackbody function is not essential. Therefore, we model the continuum X-ray spectra of XTE J1810–197 with two blackbody functions: the cooler component is most likely originating from the whole neutron star surface, while the hotter component is expected to originate from a small hot spot near the magnetic pole(s).

An accurate determination of interstellar hydrogen column density ( $nH$ ) is essential in soft X-ray spectral modeling, especially when a blackbody function is employed. In the recent study of [Alford \(2016\)](#),  $nH$  was obtained as  $0.95 \times 10^{22} \text{cm}^{-2}$  and kept constant for all their spectral analysis (using *wabs* in Xspec). Here, we employed the *tbabs* model, assuming the ISM abundance presented by [Wilms \(2000\)](#) and found that the  $nH$  values vary in a wide range covering  $0.9 - 1.5 \times 10^{22} \text{cm}^{-2}$  from 2003 to present. In order to obtain a better constrain on the this parameter and

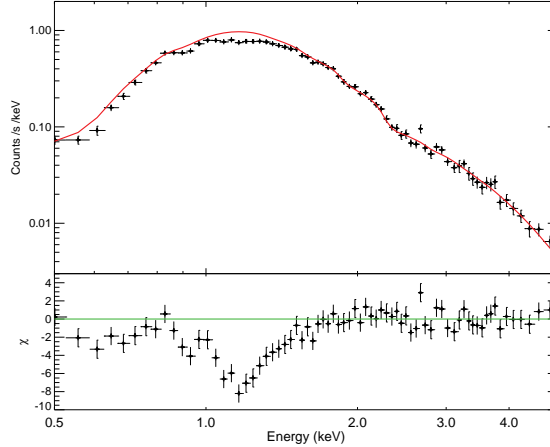


Figure 1: *Upper panel*: XMM-Newton spectrum of XTE J1810–197 as observed starting from MJD 53633.44414, and the best fit model of two blackbody functions (solid line). *Lower panel*: The residuals of the fit.

other spectral parameters, we fit the initial 17 XMM-Newton observations simultaneously by linking their  $nH$  parameter and obtain a best fit value as  $0.92 \pm 0.02 \times 10^{22} \text{cm}^{-2}$ . Assuming that the interstellar extinction remains stable, we kept the  $nH$  constant at this value throughout our spectral modeling.

We found that all 34 Chandra and XMM-Newton spectra of XTE J1810–197 were well fit with the assumed model of two blackbodies plus an asymmetric gaussian absorption: these fits yield reduced- $\chi^2$  values mainly between 0.85 and 1.4 (see Table 3 for individual values). Temperatures of the two blackbody functions evolve significantly during the first 1000 days of the outburst. The cooler blackbody component ( $kT_1$ ) started with 0.26 keV and showed a marginal increase to its maximum value of 0.29 keV then declined down to about 0.19 keV in 200 days, and remained around this constant level since then. A very similar trend is seen in the hotter blackbody component ( $kT_2$ ), which was at 0.69 keV at the onset, showing a marginal increase to the maximum value of 0.70 keV in about 400 days.  $kT_2$  then declined monotonically down to 0.5 keV in another 700 days. Since then it remained approximately constant at this value (see the first panel of Figure 2, and Table 3 for details).

We also calculated the radii of blackbody emitting regions by taking the distance to the XTE J1810–197 as  $3.1 \pm 0.5$  kpc (Durant, 2006) into account. The radius of the cold blackbody component ( $R_1$ ), on the other hand, exhibits an intriguing trend: it declined from 6 to 3 km in about 400 days after the outburst onset. Then,  $R_1$  expanded to about 7 km in another 400 days (see the second panel of Figure 2). The emitting radius of the cold component remained constant since then. The region of the hot component ( $R_2$ ) declined marginally from 0.26 to 0.20 km at the very beginning of the outburst, then remained constant at this level for almost a decade. It is likely that the location of this hot spot is near the magnetic poles.

We modeled the time evolution of the radius of the cooler blackbody component starting from about 300 days following the outburst onset, using two linear trends (see the solid line in the second panel of Figure 2). We found that the rise of the radius of the cooler blackbody component stops at around 1000 days with a maximum of about 7.5 km. The slope of the linear trend indicates a speed of spreading. After the break, the radius of this component is consistent with being nearly constant till the latest observation.

We present unabsorbed X-ray flux values in the 0.5–10.0 keV range, in the third panel of Figure 2. Flux of the colder blackbody component ( $F_1$ ) decreased slightly at the early phases of the outburst, and remains constant at around  $4 \times 10^{-12} \text{erg cm}^{-2} \text{s}^{-1}$ . Flux of the hot blackbody component ( $F_2$ ) shows an exponential decay from  $5 \times 10^{-11}$  to  $10^{-12} \text{erg cm}^{-2} \text{s}^{-1}$  during its first 1000 days. The cooling process is likely responsible for this significant decrease. In the rest of the observations,  $F_2$  fluctuates around  $10^{-12} \text{erg cm}^{-2} \text{s}^{-1}$ . Therefore, the ratio of  $F_1$  to  $F_2$  has been steady at around 4 for almost a decade.

Table 3: Fit Results of Spectral Parameters

#	kT <sub>1</sub> (keV)	Flux <sub>1</sub> <sup>†</sup>	kT <sub>2</sub> (keV)	Flux <sub>2</sub> <sup>†</sup>	Line	χ <sup>2</sup>	dof
1	0.26 ± 0.01	13.9 ± 0.4	0.69 ± 0.01	45.2 ± 0.6	asym	118.8	110
2	0.25 ± 0.03	13.9 ± 1.1	0.67 ± 0.02	44.8 ± 1.6	–	58.1	62
3	0.26 ± 0.01	12.0 ± 0.9	0.70 ± 0.01	22.9 ± 0.7	asym	120.1	107
4	0.29 ± 0.01	8.6 ± 0.3	0.70 ± 0.01	11.3 ± 0.2	asym	161.8	109
5	0.23 ± <0.01	7.5 ± 0.2	0.61 ± 0.01	5.3 ± 0.1	asym	125.1	95
6	0.21 ± <0.01	6.0 ± 0.1	0.56 ± 0.02	1.6 ± 0.1	asym	66.6	66
7	0.19 ± <0.01	5.1 ± 0.1	0.53 ± 0.02	0.9 ± <0.1	asym	56.2	54
8	0.18 ± <0.01	4.2 ± 0.1	0.45 ± 0.02	0.8 ± 0.1	–	83.3	81
9	0.18 ± <0.01	4.4 ± 0.1	0.38 ± 0.02	0.7 ± 0.1	sym	65.1	52
10	0.18 ± 0.01	4.4 ± 0.1	0.38 ± 0.03	0.5 ± 0.1	asym	37.2	45
11	0.18 ± 0.01	4.4 ± 0.1	0.36 ± 0.02	0.6 ± <0.1	asym	87.6	60
12	0.18 ± 0.01	4.0 ± 0.1	0.41 ± 0.04	0.5 ± 0.1	asym	59.1	67
13	0.19 ± <0.01	4.5 ± 0.1	0.42 ± 0.05	0.2 ± 0.1	asym	80.4	51
14	0.19 ± 0.01	4.4 ± 0.1	0.50 ± 0.08	0.2 ± 0.1	asym	65.1	34
15	0.19 ± 0.01	4.2 ± 0.2	0.40 ± 0.05	0.3 ± 0.1	asym	66.2	34
16	0.17 ± <0.01	4.1 ± 0.1	0.37 ± 0.04	0.4 ± 0.1	–	47.0	34
17	0.18 ± 0.01	4.2 ± 0.1	0.41 ± 0.04	0.5 ± 0.1	sym	66.9	60
18	0.18 ± 0.01	4.0 ± 0.2	0.49 ± 0.55	0.5 ± 0.1	–	28.1	29
19	0.17 ± 0.01	4.0 ± 0.2	0.42 ± 0.15	0.6 ± 0.1	–	26.9	30
20	0.18 ± 0.01	4.8 ± 0.3	0.42 ± 0.12	0.3 ± 0.2	asym	29.0	26
21	0.17 ± 0.01	4.3 ± 0.2	0.47 ± 0.13	0.5 ± 0.1	–	26.9	27
22	0.18 ± 0.01	4.5 ± 0.1	0.51 ± 0.44	0.2 ± 0.1	sym	29.0	26
23	0.17 ± 0.01	4.2 ± 0.2	0.46 ± 0.03	0.5 ± 0.1	asym	30.2	33
24	0.17 ± <0.01	4.3 ± 0.2	0.52 ± 0.19	0.4 ± 0.1	–	47.3	34
25	0.19 ± 0.01	4.4 ± 0.1	0.42 ± 0.10	0.2 ± 0.1	asym	40.2	33
26	0.17 ± 0.01	4.8 ± 0.1	0.42 ± 0.08	0.3 ± 0.1	asym	26.9	30
27	0.17 ± 0.01	4.0 ± 0.1	0.38 ± 0.05	0.5 ± 0.1	–	45.0	48
28	0.18 ± 0.01	4.3 ± 0.1	0.43 ± 0.06	0.4 ± 0.1	–	145.4	93
29	0.17 ± <0.01	4.4 ± 0.1	0.38 ± 0.05	0.4 ± 0.1	–	105.7	96
30	0.17 ± 0.01	4.2 ± 0.1	0.35 ± 0.12	0.4 ± 0.1	–	70.5	54
31	0.17 ± <0.01	4.4 ± 0.1	0.37 ± 0.03	0.4 ± 0.1	–	145.7	123
32	0.18 ± <0.01	4.1 ± 0.2	0.36 ± 0.01	0.6 ± 0.2	–	59.1	86
33	0.17 ± <0.01	4.1 ± 0.1	0.31 ± 0.02	0.6 ± 0.1	–	161.5	126
34	0.17 ± 0.01	4.6 ± 0.2	0.39 ± 0.04	0.5 ± 0.1	–	90.3	89

<sup>†</sup> Unabsorbed 0.5–10.0 keV flux in units of  $10^{-12}$  erg cm<sup>-2</sup> s<sup>-1</sup>.

## 5. Absorption Line

The absorption line around 1.1 keV has been reported in a number of studies of XTE J1810–197 (Alford, 2016; Bernardini, 2011; Camilo, 2016), and vaguely attributed to resonant cyclotron processes in the strongly magnetized magnetosphere. We also detected this feature in 19 out of 34 observations. It is important to note that the observed absorption feature is not always symmetric. When detected, we found that this feature is often asymmetric; it can be represented with a symmetric Gaussian profile only in a few cases. To accurately represent this feature, we introduced an asymmetric Gaussian profile where the widths of the feature is at lower and higher energies of its centroid are not necessarily the same.

In Figure 1, we present an example case where the asymmetric shape of the absorption feature can be seen clearly. To account for this fact, we include an asymmetric Gaussian function whose lower-energy half-width can be different than its higher-energy half-width. To model the detected absorption line, we construct an asymmetric Gaussian model function in *Xspec* that resembles the shape of the absorption feature. The absorption feature is observed to exhibit in certain cases a sharp decay followed by a relatively slow recovery. We define the model as

$$A(E) = \begin{cases} Ke^{\left(\frac{-(E-E_c)^2}{2\sigma_1^2}\right)}, & E < E_c \\ Ke^{\left(\frac{-(E-E_c)^2}{2\sigma_2^2}\right)}, & E \geq E_c \end{cases} \quad (3)$$

where  $K$  is the normalization,  $E_c$  is the centroid energy of the feature,  $\sigma_1$  and  $\sigma_2$  are the left and right width of the Gaussian shape, respectively. In each spectrum where the absorption feature is present, we found that the  $\sigma_1$  is

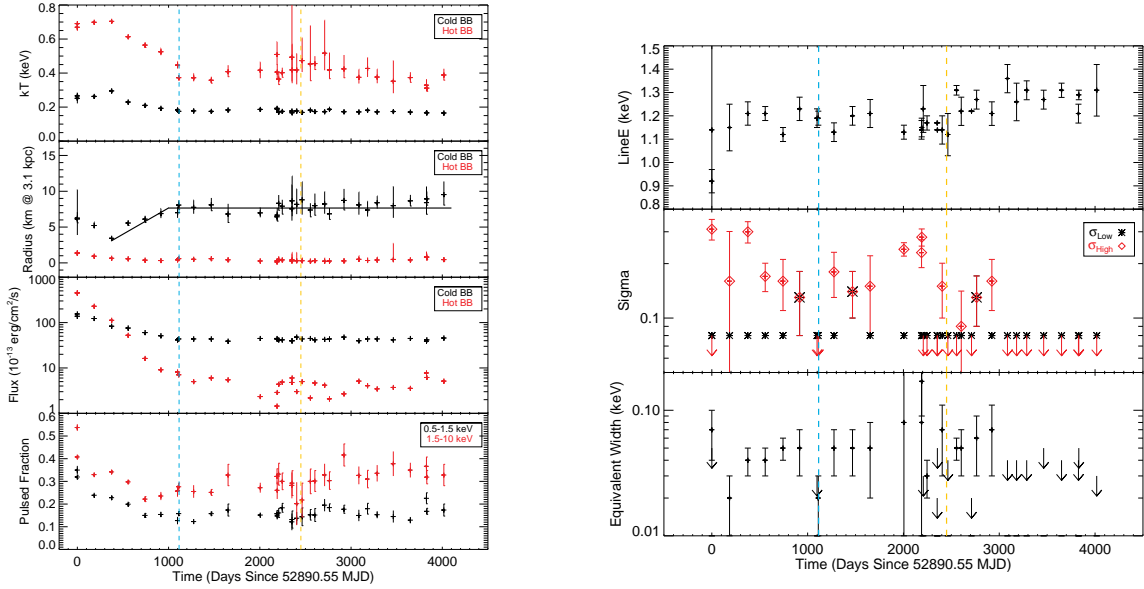


Figure 2: **Left** : Long-term evolution of the spectral model parameters and pulsed fractions. *Top panel*: Evolution of the cold and hot blackbody temperatures, *Second panel from top*: Variations of the inferred blackbody emitting radii for the two components, *Third panel from top*: Evolution of the flux of each blackbody component, and *Bottom panel*: Evolution of the pulsed fractions in the 0.5–1.5 keV energy range (black) and 1.5–10 keV (red) range. **Right** : Long-term evolution of the absorption line parameters. *First panel*: Long-term evolution of the centroid energy of absorption line energy. *Second panel*: Left and right widths of its asymmetric shape. *Last panel*: Equivalent width of the absorption line. The upside down arrow indicates upper limits. The vertical dashed blue line indicate the time of frequency change, and the dashed yellow line corresponds to the time of possible anti-glitch (Pintore, 2016).

always less than  $\sigma_2$ . We present the cases of a symmetric and an asymmetric feature in Figure 3. In the remaining 15 observations, we could only obtain upper limits to the either or both half-widths of the line feature and had to set their value to the instrumental spectral resolution limit. When fitting the line, it is not always possible to calculate the lower-energy half-width of the absorption line  $S_1$  due to the limits of the energy range. Thus, we keep  $S_1$  is fixed at 0.08 due to the minimum of the energy resolution of Chandra.

Another important issue to note is the shift in the centroid energy of the line. Apart from the very first few observation, the centroid energy of the line resides in a narrow range of 1.1 – 1.3 keV (see the top panel of Figure 2 and Table 4 for details).

The last two columns of Table 4 list  $\sigma_1^s$  and  $\sigma_2^s$  of the best fit absorption feature obtained simultaneously. We found that  $\sigma_2^s$  parameter in observations 1, 4, 13, 14, and 15 are consistent one another, and significantly larger than  $\sigma_1^s$ . To better constrain  $\sigma_2^s$  for these observations, we fitted them simultaneously by fixing the  $\sigma_1^s$  to 0.08 and linking the  $\sigma_2^s$  parameter. In the joint analysis, we allowed  $kT_1$  and  $kT_2$  for each observation float independently. As a result of this joint investigation, we determine  $\sigma_2^s$  for this group of five observations as  $0.27 \pm 0.02$  keV. Similarly,  $\sigma_2^s$  of observations of 5, 6, 7, 10, and 11 are relatively larger than  $\sigma_1^s$ . Joint spectral investigations of these observations yield an  $\sigma_2^s$  of  $0.17 \pm 0.02$  keV for this group. Finally,  $\sigma_2^s$  in observations 7, 11, and 25 are marginally larger than  $\sigma_1^s$ . The joint spectral fit results in  $0.13 \pm 0.02$  keV for them.

The equivalent width of the absorption line feature is also shown Figure 2 and indicates an overall variability

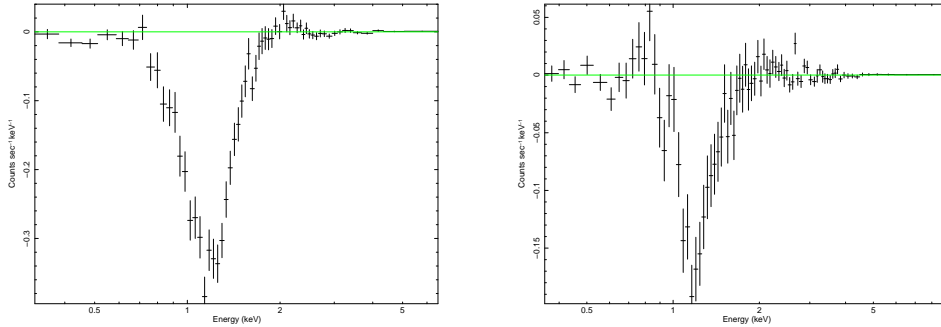


Figure 3: Sample residuals showing symmetric and asymmetric absorption line feature of XMM-Newton observations with ID: 0301270301 (*left*) and 0301270401 (*right*).

which is further discussed in the next section. Note that in a few cases the equivalent width of the feature could not be constrained.

Overall, we find that, when detected, spectral properties of the absorption feature are highly variable, and it cannot be detected in 15 observations. To better understand whether the absence of the absorption line in these 15 observations is due to the insufficient duration or decline in its X-ray flux, we have performed simulations with Xspec<sup>2</sup>. Using the continuum model employed (2 blackbody functions and an asymmetric Gaussian absorption line), we varied the X-ray flux for the values of these 15 observations, ranging from  $8.0 \times 10^{-13}$  to  $3.0 \times 10^{-11}$  erg cm<sup>-2</sup> s<sup>-1</sup>, and set exposure times at 20 ks, 40 ks and 50 ks. We found that the absorption feature is always detectable if the exposure of the observation is as large as 50 ks. Therefore, we conclude that the absence of this absorption line is not related to any instrumental effects.

## 6. Discussion and Conclusions

We investigated long-term spectral and temporal evolution of XTE J1810–197 using X-ray data collected over a long time span with Chandra and XMM-*Newton*. We modeled surface thermal evolution of XTE J1810–197 using two blackbody components of which one is most likely arising from nearly the entire neutron star surface at a temperature of 0.2 keV and the other component is a hot spot at 0.6 keV on the neutron star surface. We found that the radius of the emitting region of the cooler component is about 7 km, while that of the hot spot on the neutron star is about 0.2 km (assuming that the distance of XTE J1810–197 is  $3.1 \pm 0.5$  kpc (Durant, 2006)). Once a magnetar outburst is ignited, the release of internal magnetic energy heats up the neutron star crust most likely near or at the magnetic pole (Beloborodov, 2009). The excess heat energy on small portion of the surface (hot spot) is expected to spread and heat up a much larger portion of the surface. We found that the energy of the heated spot on the surface of XTE J1810–197 dissipates on a timescale of about 3 years, after which neither the temperatures, nor the sizes of emitting radii of both emission components change significantly. The X-ray spectra of XTE J1810–197 were previously modeled with slightly different models, such as two blackbody (Gotthelf, 2007) or three blackbody components (Alford, 2016; Bernardini, 2009). Based on our detailed numerical investigations, we found that statistically there is no requirement for a third blackbody component.

We identified two distinct emission regions; a hot spot and a much wider surface, which cools down on a much slower pace. The hot spot occupies about 0.8% of the neutron star surface area, and cools down faster while its size remain fairly constant. This is in agreement with the fact that the imparted heat energy to a small section on the surface at the onset of the outburst spreads to the whole surface of the neutron star in a time scale of a few years.

We also investigated any possible correlations between spectral and temporal properties in order to better understand the link between these quite related domains using two methods: A cross-correlation scheme and *Z-Transform*

<sup>2</sup><https://heasarc.gsfc.nasa.gov/xanadu/xspec/manual/node73.html>

Table 4: Fit Results of Line Parameters

#	Line Energy (keV)	$\sigma_1$ (keV)	$\sigma_2$ (keV)	Equivalent Width (keV)	$\sigma_1^s$ (keV)	$\sigma_2^s$ (keV)
1	$0.92 \pm 0.05$	0.08	$0.31 \pm 0.04$	$0.07 \pm 0.03$	0.08	$0.27 \pm 0.02$
2	$1.14 \pm 0.85$	0.08	0.08	<0.05		
3	$1.15 \pm 0.10$	0.08	$0.16 \pm 0.14$	$0.02 \pm 0.01$		
4	$1.21 \pm 0.05$	0.08	$0.30 \pm 0.04$	$0.04 \pm 0.01$	0.08	$0.27 \pm 0.02$
5	$1.21 \pm 0.03$	0.08	$0.17 \pm 0.03$	$0.04 \pm 0.01$	0.08	$0.17 \pm 0.02$
6	$1.12 \pm 0.03$	0.08	$0.16 \pm 0.05$	$0.05 \pm 0.01$	0.08	$0.17 \pm 0.02$
7	$1.23 \pm 0.05$	$0.13 \pm 0.05$	$0.13 \pm 0.05$	$0.05 \pm 0.02$	0.08	$0.17, 0.13 \pm 0.02$
8	$1.19 \pm 0.04$	0.08	0.08	<0.03		
9	$1.19 \pm 0.03$	0.08	0.08	$0.02 \pm 0.01$		
10	$1.13 \pm 0.04$	0.08	$0.18 \pm 0.05$	$0.05 \pm 0.02$	0.08	$0.17 \pm 0.02$
11	$1.20 \pm 0.04$	$0.14 \pm 0.04$	$0.14 \pm 0.04$	$0.05 \pm 0.02$	0.08	$0.17, 0.13 \pm 0.02$
12	$1.21 \pm 0.06$	0.08	$0.15 \pm 0.07$	$0.05 \pm 0.03$		
13	$1.13 \pm 0.03$	0.08	$0.24 \pm 0.02$	$0.08 \pm 0.12$	0.08	$0.27 \pm 0.02$
14	$1.14 \pm 0.04$	0.08	$0.23 \pm 0.04$	$0.08 \pm 0.14$	0.08	$0.27 \pm 0.02$
15	$1.15 \pm 0.04$	0.08	$0.28 \pm 0.03$	$0.17 \pm 0.08$	0.08	$0.27 \pm 0.02$
16	$1.23 \pm 0.10$	0.08	0.08	<0.03		
17	$1.17 \pm 0.03$	0.08	0.08	$0.03 \pm 0.01$		
18	1.17	0.08	0.08	<0.02		
19	1.14	0.08	0.08	<0.05		
20	$1.14 \pm 0.06$	0.08	$0.15 \pm 0.05$	$0.07 \pm 0.04$		
21	$1.12 \pm 0.09$	0.08	0.08	<0.04		
22	$1.31 \pm 0.02$	0.08	0.08	$0.05 \pm 0.01$		
23	$1.22 \pm 0.06$	0.08	$0.09 \pm 0.05$	$0.05 \pm 0.02$		
24	1.22	0.08	0.08	< 0.02		
25	$1.27 \pm 0.04$	$0.13 \pm 0.04$	$0.13 \pm 0.04$	$0.06 \pm 0.03$	0.08	$0.13 \pm 0.02$
26	$1.21 \pm 0.05$	0.08	$0.16 \pm 0.05$	$0.07 \pm 0.04$		
27	$1.36 \pm 0.06$	0.08	0.08	<0.04		
28	$1.26 \pm 0.08$	0.08	0.08	<0.04		
29	$1.31 \pm 0.04$	0.08	0.08	<0.04		
30	$1.27 \pm 0.04$	0.08	0.08	<0.05		
31	$1.31 \pm 0.03$	0.08	0.08	<0.04		
32	$1.21 \pm 0.04$	0.08	0.08	<0.04		
33	$1.29 \pm 0.02$	0.08	0.08	<0.05		
34	$1.31 \pm 0.11$	0.08	0.08	<0.03		

$\sigma_1^s$  and  $\sigma_2^s$  represents the values obtained from simultaneous fitting.

*Discrete Correlation Function (ZDCF)* (Alexander, 2013). The latter method yields the parameter errors as well. For the pulsed fractions, we employed those in the 0.5-1.5 ( $PF_{low}$ ) keV and 1.5-10.0 ( $PF_{high}$ ) keV energy range. For this examination, we considered the data for the first 1500 days. We find a strong positive correlation between the temperature of the cool blackbody and pulsed fraction in the lower energy band while the correlation between the radius of the cool blackbody is lower than the hot blackbody (see Table 5 for details). Temperature of the hot component shows a negative correlation with the pulsed fraction in the 1.5-10.0 keV band. We also computed the time lag between variations of spectral parameters and the pulsed fraction. Time lag between two parameters is important for testing models of continuum emission. Interestingly, there is a time lag between the temperatures of the blackbody components and their pulsed fraction order of days as seen in Table 5. The fluxes of the blackbody components also correlate with their pulsed fraction.

Zane (2001) points out that an absorption line at the proton cyclotron energy may exist where the line equivalent width is between 30 eV and 1 keV and the line center is located at 0.5 – 5.0 keV for field strengths  $10^{14}$ - $10^{15}$  G. Cyclotron lines are entirely important for neutron stars because of not only give a direct measurement of the magnetic field but also give information about the physical conditions of the radiating regions (Pavlov, 1991). We rigorously studied the absorption line in various ways as shown in §5. We measured that the absorption line center is located around  $\approx 1.1$  keV. Note that the line centroid shifts in energy and its profile varies between being symmetric and asymmetric. According to Özel (2001, 2003), the combination of vacuum polarization and cyclotron energy may cause such asymmetric features. In the case of strong magnetic fields, vacuum polarization affects the polarization of normal modes, alter the dielectric tensor, as well as the magnetic permeability tensor. Moreover, it also changes the interaction cross sections in the plasma.

The observed variability of the absorption feature can also be related to varying optical depth in the magnetosphere

of XTE J1810–197. Lyutikov (2006), Güver (2007) and Fernández (2007) showed that the equivalent width of a proton cyclotron line feature generated in the atmosphere of a magnetar can be affected by the optical depth in the magnetosphere. We conclude that the variation of the equivalent width of the line could be attributed to variations in optical depth in the magnetosphere, likely due to loading or unloading particles in the line of sight. Therefore, the line feature might get smeared in the case of higher particle density, while reappears when the density drops. Bignami (2003) also stress that in the cyclotron scattering above the surface, cross-section depends on the angle between observer and magnetic axis. This yields to a variation of the feature depth. The line-width also vary if the observer’s line of sight and the magnetic field are perpendicular.

In a recent study, Pintore (2016) demonstrated that there exist timing irregularities in the spin period evolution of XTE J1810–197 the one around MJD 55400 was interpreted as an anti-glitch. They also noted a frequency change around MJD 54000. On the other hand, we marked these particular times in Figure 2. We find that the time of frequency change is somehow coincident with spectral and temporal alterations for both hot and cold BB components. We find no radiative changes in it emission at the time of suggested anti-glitch. This is consistent with the anti-glitch observed from 1E 1841-045 (Şaşmaz Muş, 2014), while both anti-glitch sources differ from 1E 2259+586 in which the anti-glitch was associated with clear flux enhancement (Archibald, 2013).

Table 5: Correlations between Pulsed Fractions and Spectral Parameters for the first 1500 days

Parameter Pairs	ZDCF (0.5-10.0 keV)	Time Lag (days) (0.5-10.0 keV)	Correlation Coefficient	Time Lag (days)
$kT_1 - PF_{low}$	$0.90^{+0.04}_{-0.04}$	$312^{+55}_{-71}$	0.775	-360
$R_1 - PF_{low}$	$-0.77^{+0.09}_{-0.08}$	$312^{+70}_{-55}$	-0.859	-360
$F_1 - PF_{low}$	$0.95^{+0.03}_{-0.04}$	$26^{+24}_{-27}$	0.941	0
$kT_2 - PF_{high}$	$-0.70^{+0.13}_{-0.11}$	$693^{+67}_{-40}$	0.695	-360
$R_2 - PF_{high}$	$0.79^{+0.10}_{-0.14}$	$26^{+24}_{-27}$	0.935	0
$F_2 - PF_{high}$	$0.84^{+0.08}_{-0.11}$	$26^{+24}_{-27}$	0.846	0

## 7. Acknowledgements

We thank the anonymous referee for constructive comments. EV thanks Armin Vahdat Motlagh for his help and useful discussions. We thank Muhammed Diyaddin Ilhan for his help in the ZDCF analysis. This work was supported by Scientific Research Project Coordination Unit of Istanbul University with project numbers: 57462, 48934. EV has been supported by the Scientific and Technological Research Council (TUBITAK) through project 113F270. This research has made use of data obtained from the High Energy Astrophysics Science Archive Research Center (HEASARC), provided by NASA’s Goddard Space Flight Center.

## References

- Alexander, T. 2013, preprint, [arXiv:1302.1508](https://arxiv.org/abs/1302.1508)
- Archibald, R. F., Kaspi, V. M., Ng, C., Gourgouliatos, K. N., Tsang, D., Scholz, P., Beardmore, A. P., Gehrels, N. and Kennea, J. A. 2013, *AAS/High Energy Astrophysics Division*, 103.09
- Alford, J. A. J. and Halpern, J. P. 2016, *ApJ*, **818**, 122
- Arnaud, K. A. 1996, *Astronomical Society of the Pacific Conference Series*, Vol.101, *Astronomical Data Analysis Software and Systems V*.p. 17
- Beloborodov, A. M. 2009, *ApJ*, **703**, 1044
- Bernardini, F., Israel, G. L., Dall’Osso, S., Stella, L., Rea, N., Zane, S., Turolla, R., Perna, R., Falanga, M., Campana, S., Götz, D., Mereghetti, S. and Tiengo, A. 2009, *A&A*, **498**, 195
- Bernardini, F., Perna, R., Gotthelf, E. V., Israel, G. L., Rea, N. and Stella, L. 2011, *MNRAS*, **418**, 638
- Bignami, G.F., Caraveo, P.A., De Luca, A., Mereghetti, S. 2003, *Nature*
- Buccheri, R., Bennett, K., Bignami, G. F., Bloemen, J. B. G. M., Boriakoff, V., Caraveo, P. A., Hermsen, W., Kanbach, G., Manchester, R. N., Masnou, J. L., Mayer-Hasselwander, H. A., Ozel, M. E., Paul, J. A., Sacco, B., Scarsi, L., Strong, A. W. 1983, *A&A*, **128**, 245
- Camilo, F., Ransom, S. M., Halpern, J.P., Alford, J.A. J., Cognard, I., Reynolds, J.E., Johnston, S., Sarkissian, J., van Straten, W. 2016, *ApJ*, **820**, 2
- Duncan, R. C., Thompson C. 1992, *ApJ*, **392**, L9
- Duncan, R. C., Thompson C. 1996, *AIP Conference Proceedings* **366**, 111
- Durant, M. and van Kerkwijk, M. H. 2006, *ApJ*, **650**, 1070

Fernández, R. and Thompson, C. 2007, [ApJ](#), **660**, 615  
Gotthelf, E. V. and Halpern, J. P. 2007, [Ap & SS](#), **308**, 79  
Göğüş, E., Woods, P. M., Kouveliotou, C., Kaneko, Y., Gaensler, B. M., Chatterjee, S. 2010, [ApJ](#), **722**, 899  
Güver, T., Özel, F., Göğüş, E. and Kouveliotou, C. 2007, [ApJ](#), **667**, L73  
Halpern, J. P., Gotthelf, E. V., Becker, R. H., Helfand, D. J., White, R. L. 2005, [ApJ](#), **632**, L29  
Helfand, D. J., Chatterjee, S., Brisken, W. F., Camilo, F., Reynolds, J., van Kerkwijk, M. H., Halpern, J. P., Ransom, S. M. 2007, [ApJ](#), **662**, 1198  
Ibrahim, A. I., Markwardt, C. B., Swank, J. H., Ransom, S., Roberts, M., Kaspi, V., Woods, P. M., Safi-Harb, S., Balman, S., Parke, W. C., Kouveliotou, C., Hurley, K., Cline, T. 2004, [ApJ](#), **609**, L21  
Kaspi, V. M. 2007, [Ap & SS](#), **308**, 1  
Lytikov, M. and Gavriil, F. P. 2006, [MNRAS](#), **368**, 690  
Olausen, S. A. and Kaspi, V. M. 2014, [VizieR Online Data Catalog](#), 221  
Özel, F. 2001, [ApJ](#), **563**, 276  
Özel, F. 2003, [ApJ](#), **583**, 402  
Pavlov, G.G., Bezchastnov, V.G., Meszaros, P., Alexander, S.G. 1991, [ApJ](#), **380**, 541  
Pintore, F., Bernardini, F., Mereghetti, S., Esposito, P., Turolla, R., Rea, N., Zelati, F. C., Israel, G. L., Tiengo, A., Zane, S. 2016, [MNRAS](#), **458**, 2  
Wilms, J., Allen, A. and McCray, R. 2000, [ApJ](#), **542**, 914  
Şaşmaz Muş, S., Aydın, B. and Göğüş, E. 2014, [MNRAS](#), **440**, 2916  
Zane, S., Turolla, R., Stella, R. and Treves, A. 2001, [ApJ](#), **560**, 384-389